JOURNAL OF COMPUTATIONAL PHYSICS **130,** 54–66 (1997)
ARTICLE NO. CP965475

Characterization of the Darwin Direct Implicit Particle-in-Cell Method and Resulting Guidelines for Operation[1]

Matthew R. Gibbons and Dennis W. Hewett

Lawrence Livermore National Laboratory, Livermore, California 94551

Received December 12, 1994; revised December 4, 1995

We investigate the linear dispersion and other properties of the Darwin Direct Implicit Particle-in-cell (DADIPIC) method in order to deduce guidelines for its use in the simulation of long time-scale, kinetic phenomena in plasmas. The Darwin part of this algorithm eliminates the Courant constraint for light propagation across a grid cell in a time step and divides the field solution into several elliptic equations. The direct implicit method is only applied to the electrostatic field relieving the need to resolve plasma oscillations. Linear theory and simulations verifying the theory are used to generate the desired guidelines as well as show the utility of DADIPIC for a wide range of low frequency, electromagnetic phenomena. We find that separation of the fields has made the task of predicting algorithm behavior easier and produced a robust method without restrictive constraints.

I. INTRODUCTION

In a previous paper [1] we introduced the Darwin direct implicit particle-in-cell (DADIPIC) method which eliminates the constraints $c\Delta x/\Delta t < 1$ and $\omega_{pe}\Delta t < 2$ on electrodynamic PIC simulation. In that paper we discussed the details of the numerical implementation of field solutions and particle advances including boundary conditions. Here we present the performance of DADIPIC and guidelines for its application to low frequency, kinetic plasma phenomena. The foundation of DADIPIC is the combination of the Darwin and direct implicit methods. The Darwin method is a reduction of Maxwell's equations to a radiation free limit thus removing the light propagation Courant condition. The direct implicit method works with the finite difference equations in an implicit form and is used to solve for a time-advanced electrostatic field. In this way the unresolved plasma oscillations are numerically damped out and are no longer a source of instability.

DADIPIC is characterized in this paper by answering the following questions. Are spatially and temporally resolved plasma phenomena simulated accurately? What is the response of the method when the above Courant and plasma frequency conditions are not met? Are there numerical constraints on the algorithm as presently implemented? What improvements can be made to the method? We believe that the answers to these questions show DADIPIC to be a robust algorithm for the simulation of low frequency phenomena in unbounded or bounded plasmas. An overview of the DADIPIC method is presented in Section II. Section III has guidelines for the application of DADIPIC based on theory for its expected operation. Section IV shows the actual performance of the method in 2D as Δx and Δt are varied both as verification of theory and proof of robustness under stressful circumstances. In Section V the guidelines found in Sections III and IV are condensed into a region of operation for stable and accurate DADIPIC simulation.

II. IMPLEMENTATION OF DARWIN DIRECT IMPLICIT PARTICLE-IN-CELL

Our implementation of DADIPIC results in an algorithm in which the implicit electrostatic field and the Darwin magnetoinductive fields are found separately. We will describe the calculation of the fields and then present the algorithm which combines Darwin fields with the implicit particle advance.

A. Implicit Electrostatic Method

Implicit methods achieve stability by including information from the next time step in the equations for the time

[1] This document was prepared as an account of work sponsored by an agency of the United States Government. Neither the United States Government nor the University of California nor any of their employees, makes any warranty, express or implied, or assumes any legal liability or responsibility for the accuracy, completeness, or usefulness of any information, apparatus, product, or process disclosed, or represents that its use would not infringe privately owned rights. Reference herein to any specific commercial products, process, or service by trade name, trademark, manufacturer, or otherwise, does not necessarily constitute or imply its endorsement, recommendation, or favoring by the United States Government or the University of California. The views and opinions of authors expressed herein do not necessarily state or reflect those of the United States Government or the University of California and shall not be used for advertising or product endorsement purposes. The U.S. Government's right to retain a nonexclusive royalty-free license in and to the copyright covering this paper, for governmental purposes, is acknowledged.

0021-9991/97 $25.00

advance of present quantities. An overview of the Direct Implicit method including electromagnetics and energy conservation characteristics can be found in Langdon and Barnes [2]. In this algorithm the particles are time integrated according to the D_1 implicit scheme [3] which causes large damping of high frequency oscillations while retaining low frequency phenomena. The finite differenced equations take the form

$$\begin{aligned}\mathbf{v}^{n+1/2} &= \mathbf{R}^n \cdot \mathbf{v}^{n-1/2} + \frac{\Delta t}{2m}(\mathbf{I} + \mathbf{R}^n) \cdot \left(\frac{q}{m}\mathbf{E}^n_{\text{sol}} + \bar{\mathbf{a}}^n\right)\\ \mathbf{x}^{n+1} &= \mathbf{x}^n + \Delta t \mathbf{v}^{n+1/2}\\ \bar{\mathbf{a}}^n &= \frac{1}{2}\left[\bar{\mathbf{a}}^{n-1} + \frac{q}{m}\mathbf{E}^{n+1}_{\text{irr}}\right],\end{aligned} \tag{2.1}$$

where $\mathbf{E}_{\text{sol}}$ is the solenoidal part of the field, and $\mathbf{E}_{\text{irr}}$ is the irrotational part of the field. In Eq. (2.1) $\mathbf{I}$ is the identity tensor and $\mathbf{R}$, the rotation due to $\mathbf{v} \times \mathbf{B}$, is given by

$$\begin{aligned}\mathbf{R}^n &= [(1 - (\Theta^n)^2)\mathbf{I} - 2\Theta^n \times \mathbf{I} + 2\Theta^n\Theta^n]/(1 + (\Theta^n)^2)\\ \Theta^n &= q\mathbf{B}^n \Delta t/2mc.\end{aligned} \tag{2.2}$$

Notice that $\bar{\mathbf{a}}$ carries only the time advanced electrostatic field. Unlike other electromagnetic implicit algorithms, the particle push is still explicit with respect to $\mathbf{E}_{\text{sol}}$ and $\mathbf{B}$. So a time advanced field solve must only be found for $\mathbf{E}_{\text{irr}}$. This particle push is broken up into two steps [5]. The first push uses only known quantities to advance $\mathbf{v}$ and $\mathbf{x}$ to a $\sim$ level, and the $\sim$ quantities are used to estimate the advanced $\mathbf{E}_{\text{irr}}$. The predicted $\mathbf{E}_{\text{irr}}$ is then used to complete the advance to the n + 1 time step.

Using the notation of Eq. (2.1), the intermediate quantities for each particle are

$$\begin{aligned}\tilde{\mathbf{v}} &= \mathbf{R}^n \cdot \mathbf{v}^{n-1/2} + \frac{\Delta t}{2}(\mathbf{I} + \mathbf{R}^n) \cdot \left(\frac{q}{m}\mathbf{E}^n_{\text{sol}} + \frac{1}{2}\bar{\mathbf{a}}^{n-1}\right)\\ \tilde{\mathbf{x}} &= \mathbf{x}^n + \Delta t \tilde{\mathbf{v}}.\end{aligned} \tag{2.3}$$

The final positions and velocities are obtained from

$$\begin{aligned}\mathbf{v}^{n+1/2} &= \tilde{\mathbf{v}} + \delta\mathbf{v}\\ \mathbf{x}^{n+1} &= \tilde{\mathbf{x}} + \Delta t \delta\mathbf{v}\\ \delta\mathbf{v}(\mathbf{x}^n, \mathbf{x}^{n+1}) &= \frac{q\Delta t}{4m}(\mathbf{I} + \mathbf{R}^n)\mathbf{E}^{n+1}_{\text{irr}}(\mathbf{x}^{n+1}).\end{aligned} \tag{2.4}$$

With this scheme $\delta\mathbf{v}$ cannot be found until the advanced $\mathbf{E}_{\text{irr}}$ is estimated. An approximate field equation is obtained by taking a Taylor expansion of the accumulated charge density at time n + 1 about $\tilde{\mathbf{x}}$. The result using simplified differencing [3] can be written in terms of the time advanced electrostatic field,

$$\begin{aligned}\rho^{n+1} &= \tilde{\rho} - \nabla \cdot (\mathbf{X} \cdot \mathbf{E}^{n+1}_{\text{irr}})\\ \mathbf{X} &= \frac{\Delta t^2}{4}\sum_s (\mathbf{I} + \mathbf{R}^n)\left[\frac{q_s\tilde{\rho}_s}{m_s}\right],\end{aligned} \tag{2.5}$$

where the sum is over species of particles. The $\mathbf{X}$ tensor is formed from the B-field and charge density already stored on the grid. This differencing provides a significant reduction in computation since it avoids extra interpolation of particle quantities to the grid and leads to a simpler finite difference field solution. With the simplified differencing expression for ρ^{n+1} the field equation becomes

$$\nabla \cdot [(\mathbf{I} + 4\pi\mathbf{X})\nabla\phi^{n+1}] = 4\pi\tilde{\rho}. \tag{2.6}$$

In 2D this equation has a nine-point template of coefficients in the solution matrix for each potential node to be solved.

B. Darwin Method

The Darwin limit is the minimum reduction in Maxwell's equations necessary to eliminate the propagation of light waves [6]. An overview of the Darwin method can be found in Nielson and Lewis [7]. The method eliminates the CFL constraint on light propagation while retaining all kinetic effects for the particles in the radiation free fields. The Darwin field equations also reduce the size of electromagnetic fluctuations compared to fully electromagnetic codes [7] allowing the use of fewer particles.

The essence of this radiation free limit is obtained by ignoring the solenoidal part of the displacement current in Ampere's law. Maxwell's equations can then be reformulated into the following set of elliptic equations where the time advance is carried solely by the particle quantities [1, 7]. For the electrostatic potential Poisson's equation in the modified form of Eq. (2.6) is used to allow an implicit particle advance with respect to the electorstatic field. In a 2D code two forms are used to solve for the B-field in order to ensure that $\nabla \cdot \mathbf{B} = 0$ and $\nabla \cdot \mathbf{A} = 0$. The component of $\mathbf{B}$ which is out of the simulation plane is given by

$$\nabla^2 B_y = -\frac{4\pi}{c}(\nabla \times J)_y. \tag{2.7}$$

The second equation is obtained by replacing $\mathbf{B}$ with its vector potential form

$$\nabla^2 A_y = -\frac{4\pi}{c} J_{\text{sol},y}. \tag{2.8}$$

Finally, the combination of the two curl equations gives

$$\nabla^2 \mathbf{E}_{\text{sol}} = \frac{4\pi}{c^2} \mathbf{j}_{\text{sol}}. \tag{2.9}$$

The streamlined Darwin field (SDF) formulation is used to avoid both boundary condition and vector decomposition problems in solving Eq. (2.9) [1, 8].

C. Combined Algorithm

As explained in Gibbons and Hewett [1], the field solutions of Sections II.A and II.B are integrated into a combined algorithm for the time advance of particle and field quantities. Given initial values of $\mathbf{E}_j^n$, $\mathbf{B}_j^n$, $\mathbf{x}_i^n$, $\mathbf{v}_i^{n-1/2}$, and $\overline{\mathbf{a}}_i^{n-1}$ with j designating grid quantities and i particle quantities, the procedure is as follows:

I. Advance to $\sim$ level.

(1) Interpolate $\mathbf{E}_{\text{sol},j}^n$ and $\mathbf{B}_j^n$ to the particles.

(2) Push particles to $\tilde{\mathbf{v}}_i$ and $\tilde{\mathbf{x}}_i$ using Eqs. (2.3).

(3) Interpolate the $\tilde{\mathbf{v}}_i$ and $\tilde{\mathbf{x}}_i$ to the grid to get $\tilde{\rho}_j$ and $\mathbf{X}_j$.

(4) Solve the implicit electrostatic field Eq. (2.6) to find $\mathbf{E}_{\text{irr},j}^{n+1}$.

II. Advance to n + 1 level.

(1a) Interpolate $\mathbf{E}_{\text{irr},j}^{n+1}$, and $\mathbf{B}_j^n$ to the particles.

(2a) Push particles to $\mathbf{v}_i^{n+1/2}$ and $\mathbf{x}_i^{n+1}$ using Eqs. (2.4), evaluate $\delta\mathbf{v}$ at $\tilde{\mathbf{x}}_i$, and save $\overline{\mathbf{a}}_i^n$.

(1b) Interpolate $\mathbf{E}_{\text{irr},j}^{n+1}$, $\mathbf{E}_{\text{sol},j}^n$, and $\mathbf{B}_j^n$ to the particles.

(2b) Find $\mathbf{v}_i^{n+1}$ from

$$\mathbf{v}_i^{n+1} = \mathbf{R}^n \cdot \mathbf{v}_i^{n+1/2} + \frac{q\Delta t}{4m} (\mathbf{I} + \mathbf{R}^n) \cdot (\mathbf{E}_{\text{irr}}^{n+1} + \mathbf{E}_{\text{sol}}^n). \tag{2.10}$$

(3) Interpolate the $\mathbf{v}_i^{n+1}$ and $\mathbf{x}_i^{n+1}$ to the grid to get $\mathbf{J}_j^{n+1}$, ρ_j^{n+1}, and $\mathbf{K}_j^{n+1}$.

(4) Solve the **B**-field and SDF Eqs. (2.7), (2.8), and (2.9) to find $\mathbf{B}_j^{n+1}$ and $\mathbf{E}_{\text{sol},j}^{n+1}$.

III. THEORY OF DADIPIC OPERATION

A. Effect of the Direct Implicit Method

Several sources discuss the effect of finite spatial and temporal discretization on the direct method [2–4]. This section is a summary of the constraints to be met for accurate solution of the field equation.

First we must consider whether Eq. (2.5) is a reasonable approximation of ρ^{n+1}. For a linear shape function it is exact as long as the particle remains within the cell in which it started or

$$\frac{\delta\mathbf{v}\Delta t}{\Delta x} = \frac{q\Delta t^2}{4m\Delta x} (\mathbf{I} + \mathbf{R})\mathbf{E} \ll 1. \tag{3.1}$$

The evaluation of Eq. (2.5) at $\tilde{\mathbf{x}}$ further restricts the predictor term to only be accurate for **R** and **E** which have scale lengths long compared to $\Delta t\delta\mathbf{v}$. Since the gridding limits the variation of these quantities, the constraint of Eq. (3.1) should be sufficient. For higher order shape functions the other terms in the expansion have been neglected, but again constraint (3.1) would cause these terms to be small. Under conditions where Eq. (3.1) is a valid expansion, we can expect an accurate solution from the electrostatic field equation with strict differencing. The minimum density fluctuation scale lengths for which the simplified differencing of Eq. (2.5) agrees with strict differencing are found to be on the order of a few grid cells [4].

An estimate of the time step needed to resolve a phenomena with frequency ω_o can be found from a von Neumann stability analysis of the time-advance difference equations, assuming a time harmonic oscillation of only the electrostatic field [9]. This results in a dispersion relation for the normal modes at ω dependent on the driven frequency ω_o. For the D_1 implicit scheme the dispersion relation is [3]

$$(\omega_o\Delta t)^2 z^3 + (2z - 1)(z - 1^2) = 0, \tag{3.2}$$

where $z = \exp(-i\omega t)$. $\|z\|$ for the least damped simple-harmonic oscillator mode shows large damping for large $\omega_o\Delta t$; however, the damping is quite small for $(\omega_o\Delta t)^2$ less than .05. Thus the constraints for resolving electrostatic phenomena are Eq. (3.1) and

$$k\Delta x \leq 1, \quad \omega_o\Delta t \leq .2 \tag{3.3}$$

B. Effect of the B-Field on the Implicit Electrostatic Field Equation Matrix

Because of the explicit advance with respect to the B-field, certain constraints on the time step occur in relation to the electron gyrofrequency, ω_{ce}. We must consider the implicit electrostatic field equation since the rotation tensor depends on the B-field. A condition to ensure a nonsingular implicit field solution matrix is found from the theorem [10]:

Let M and C be $n \times m$ matrices with M being nonsingular and let $\|\cdot\|$ denote any of the operator norms. If $\alpha = \|M^{-1}C\| < 1$ (or $a = \|CM^{-1}\| < 1$) then $M + C$ is nonsingular.

The field matrix can be analyzed to find the constraint on Δt necessary for this condition to be met. In order to simplify the analysis without significant effects on the constraint, consider a uninform plasma with doubly periodic boundaries and with B_x and B_z comparable. Assuming only small perturbation in the density, the X tensor and matrix coefficients simplify to

$$4\pi \mathrm{X}^{ii} = \frac{(\omega_p\Delta t)^2}{4} [1 + (1 - \theta^2 + 2\theta_i^2)/(1 + \theta^2)]$$

$$4\pi X^{ij} = \frac{(\omega_p \Delta t)^2}{4}\left[2(\theta_i\theta_y + \theta_j)/(1+\theta^2)\right]$$

$$\text{diagonal term} \approx \frac{4}{\Delta^2}(1 + X^{xx})$$

$$\begin{matrix}\text{nine-point template}\\ \text{side terms}\end{matrix} \approx \frac{1}{\Delta^2}(1 + X^{xx})$$

$$\begin{matrix}\text{nine-point template}\\ \text{corner terms}\end{matrix} \approx \frac{1}{4\Delta^2}(X^{xz} + X^{zx}). \tag{3.4}$$

Now split the matrix into two parts so $A = M + C$. Let M contain the five-point template, and C contain the corner coefficients of the nine-point template. Factoring the variables from M and C, the matrices take the form

$$M = \frac{1 + X^{xx}}{\Delta^2}\begin{pmatrix} -4 & 1 & 0 & 0 & \dots \\ 1 & -4 & 1 & 0 & \dots \\ 0 & 1 & -4 & 1 & \dots \\ 0 & 0 & 1 & -4 & \dots \\ \vdots & \vdots & \vdots & \vdots & \ddots \end{pmatrix}$$

$$= \frac{1 + X^{xx}}{\Delta^2}\tilde{M} \tag{3.5}$$

$$C = \frac{X^{xz} + X^{zx}}{4\Delta^2}\begin{pmatrix}\text{sparse matrix}\\ \text{of ones}\end{pmatrix} = \frac{X^{xz} + X^{xz}}{4\Delta^2}\tilde{C}; \tag{3.6}$$

thus

$$\|M^{-1}C\| = \frac{X^{xz} + X^{zx}}{4(1 + X^{xx})}\|\tilde{M}^{-1}\tilde{C}\|. \tag{3.7}$$

The assumption $\omega_{pe}\Delta t \gg 1$ leads to the most restrictive constraint. In addition for all components of θ approximately the same and $\alpha = \|\tilde{M}^{-1}\tilde{C}\|$, the matrix is nonsingular if

$$\frac{\theta^2 + \theta}{2(1+\theta^2)}\alpha < 1. \tag{3.8}$$

Solving for θ, the constraint on Δt is

$$\omega_{ce}\Delta t < \frac{-\alpha + \sqrt{\alpha^2 + 8(\alpha - 2)}}{\alpha - 2}. \tag{3.9}$$

The norm $\|\tilde{M}^{-1}\tilde{C}\|$ was solved numerically for different sized problems. Figure 1 shows the results for an $n \times n$ grid. Large enough grids might eventually impose a more restrictive constraint than that needed to resolve cyclotron oscillations. While violating the constraint will not necessarily result in a singular matrix, meeting the constraint does guarantee a nonsingular matrix.

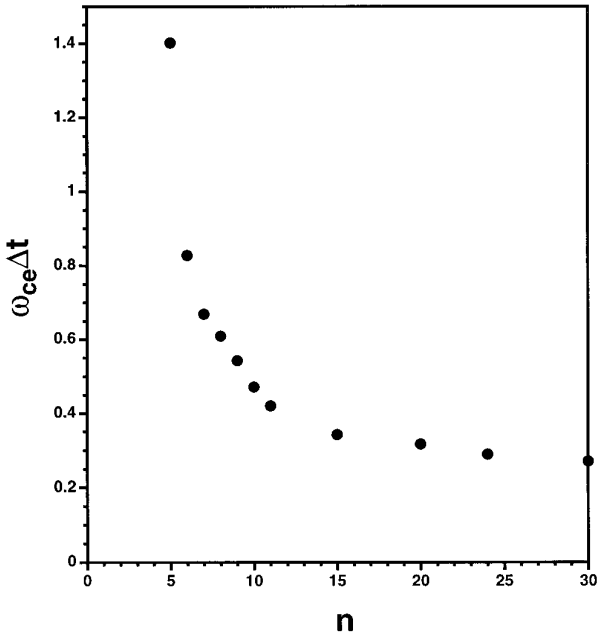

FIG. 1. Maximum $\omega_{ce}\Delta t$ to guarantee nonsingular matrix for the implicit electrostatic field equation. This is a sufficient but not necessary condition.

C. Effect of the Darwin Method

Linear theory gives the dispersion characteristics of the Darwin limit in plasma. As expected longitudinal waves, such as plasma oscillations, are unaffected. However, the absence of the solenoidal part of the displacement current does have major consequences for transverse waves. Fast waves (those with phase velocities larger than c) are nonpropagating. For example in a Darwin plasma with no imposed fields the dispersion relation for transverse waves is $-c^2k^2 = \omega_{pe}^2(1 + Zm_e/m_i)$. This results in imaginary k or spatially damped fields. The magnitude of the effect on slow waves depends on the plasma characteristics. As discussed by Kaufman and Rostler [11], in a magnetized plasma $(ck/\omega)^2_{\text{Darwin}} \sim (ck/\omega)^2_{\text{Maxwell}} - 1$. So Darwin is best used for those phenomena where transverse wave velocities as well as particle velocities are significantly less than the speed of light.

A constraint on time step occurs for the numerical Darwin plasma with an imposed B-field. This can be seen in the dispersion relation for a neutral, magnetized plasma in which we neglect electrostatic fields and follow the fluid

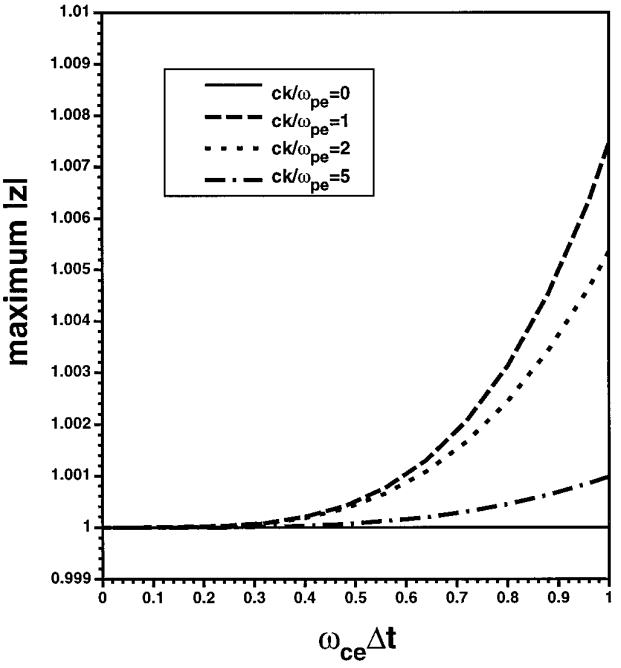

FIG. 2. Magnitude of the least damped mode versus $\omega_{ce}\Delta t$ from the linear analysis of the Darwin field equation and finite difference equations of motion in a constant B-field.

motion of the numerical plasma. A B-field is applied in the z direction, and we will consider spatial variation only in z. The linearized finite difference Eqs. (2.1), (2.10), and (2.9) become

$$\mathbf{V}^{n+1/2} = \mathbf{V}^{n-1/2} + \frac{\Delta t q}{m}\left(\mathbf{E}^n + \frac{\mathbf{V}^{n+1/2} + \mathbf{V}^{n-1/2}}{2c} \times B_o\hat{z}\right) \quad (3.10)$$

$$\mathbf{V}^{n+1} = \mathbf{V}^{n+1/2} + \frac{\Delta t q}{2m}\left(\mathbf{E}^n + \frac{\mathbf{V}^{n+1} + \mathbf{V}^{n+1/2}}{2c} \times B_o\hat{z}\right) \quad (3.11)$$

$$-(k^2 + \omega_{pe}^2/c^2)\mathbf{E}^{n+1} = \frac{\omega_{pe}^2}{c^3}\mathbf{V}^{n+1} \times B_o\hat{z}. \quad (3.12)$$

Splitting these into components for V_x and V_y, results in six equations and eight unknowns. Assuming time harmonic variation, $z = \exp(-i\omega\Delta t)$, for all quantities, the system can be reduced to two equations and two unknowns. Setting the determinant of the 2×2 matrix to zero gives the dispersion relation

$$\begin{aligned}&\lambda^2(1+\alpha^2)(1+4\alpha^2)z^4 - 2\\ &\quad[\lambda^2(1+\alpha^2)(1-4\alpha^2) + 18\lambda\alpha^2]z^3\\ &\quad+ [\lambda^2(1+\alpha^2(1+4\alpha^2) + 8\lambda\alpha^2(1-2\alpha^2) + 36\alpha^2]z^2\\ &\quad- 4\alpha^2[\lambda(1+4\alpha^2)+6]z + 4\alpha^2(1+4\alpha^2) = 0 \end{aligned} \quad (3.13)$$

where $\alpha = \omega_{ce}\Delta t/4$ and $\lambda = 1 + (ck/\omega_{pe})^2$. The magnitude of z versus $\omega_{ce}\Delta t$ is plotted in Fig. 2 for various ck/ω_{pe}. $\|z\|$ is larger than one which indicates instability. However, even in the worst case when $ck/\omega_{pe} \simeq 1$, $\|z\| = 1.0002$ for $\omega_{ce}\Delta t = 0.4$. For applications without large, imposed B-fields $\omega_{ce}\Delta t$ is usually much less than 0.4, and the number of time steps before this instability grows significantly is more than required by the simulation. This analysis is also overly conservative for those cases where there is no static imposed field. See Section IV for further discussion of our experience with simulations having imposed B-fields.

D. Electrostatic and Electromagnetic Field Fluctuations

While the above constraints for resolving low frequency phenomena are met, the high frequency plasma oscillations which cause the unavoidable fluctuation background in the plasma are probably not resolved. Most studies of the numerical dispersion effects of the implicit method have concentrated on the electrostatic field. Since the electromagnetic fluctuation fields are much smaller than the electrostatic fluctuations fields, the numerical effects of the EM fluctuation fields should be relatively small. In Section IV the validity of this assumption is investigated.

The change in the total kinetic energy density of the plasma particle distribution is

$$\frac{d\langle K\,E\rangle}{dt} = n_o \int d\mathbf{x} \int d\mathbf{v}\, \frac{\partial f}{\partial t}\frac{1}{2}mv^2. \quad (3.14)$$

For the continuum plasma a Maxwellian distribution is an equilibrium (i.e., Eq. (3.14) gives zero). It has been known for some time and quantified with computations that the uniform, Maxwellian PIC plasma does suffer a continuous change in energy [13]. Langdon used kinetic theory to find the terms in the Fokker–Planck equation to give a functional form for the electrostatic PIC plasma $d\langle K\,E\rangle/dt$ [14]. The function is directly proportional to the number of actual particles per simulation particle, N_o/N_p, and has arguments of $\Delta x/\lambda_D$ and $\omega_p\Delta t$ or

$$\frac{d\langle K\,E\rangle}{dt} = n_o\frac{N_o}{N_p}G(\Delta x/\lambda_D, \omega_p\Delta t). \quad (3.15)$$

It is shown that explicit methods would cause only heating of the plasma while implicit methods could also cause cooling for some Δx and Δt [15]. In DADIPIC there is a coupling of an implicit electrostatic field solution with an explicit magneto-inductive field solution. From Eq. (3.15) one can see that a set of simulations of uniform plasma at different $\Delta x/\lambda_D$ and $\omega_p\Delta t$ with N_o/N_p constant would give a contour plot of G. The energy change in any simulation could then be found from n_o and N_o/N_p of that particular simulation. The plot should also hold for nonuniform plasmas with electromagnetic phenomena other than fluctua-

tions as long as the other phenomena are well resolved spatially and temporally.

IV. CHARACTERIZATION OF DADIPIC WITH DOUBLY PERIODIC TEST CASES

Several test cases follow which characterize the accuracy and robustness of DADIPIC under circumstances that are increasingly stressful to the algorithm. The simulations are doubly periodic to investigate the core algorithm without the effects of boundaries. We begin with a uniform, Maxwellian plasma to determine the numerical effects on what should be an equilibrium situation. The plasma is magnetized to check the applicability of the Darwin dispersion results. Finally, the reaction of the algorithm to large density gradients coupled with an electromagnetic instability is tested.

A. Uniform Plasma: Change in Energy due to Fluctuations

1. *Simulation Parameters and Timings*

Here we present the results of a set of simulations as suggested in Section III to find the form of the function in Eq. (3.15) for the change in kinetic energy of the DADIPIC plasma due to fluctuations. A set of 28 simulations with 32×32 cells were initialized with 30,000 particles each of electrons and protons at a density of 10^8cm^{-3}. The size of the problem was set at 1 cm^2. The plasma temperature ($T_e = T_i$) and time step were varied to get desired values for $\Delta x/\lambda_{DE}$ and $\omega_{pe}\Delta t$ ranging from 0.2 to 20.

Figure 3 is a set of typical time histories for the particle and field energies. Notice that the initial relaxation of the field energy occurs quickly in the first few time steps, followed by a general trend of heating or cooling. In the simulations the field energy represented only a small fraction of the total energy, and the ions showed almost no change from their initial kinetic energy. For all practical purposes the change in energy was due to the change in the thermal energy of the electrons in the x and z directions. In these 2D simulations there is no electrostatic field in the y direction, and the fluctuation electromagnetic fields had no perceptible impact on the particle kinetic energy in the y direction.

Several trends in the field and particle energies occur. As $\Delta x/\lambda_{De}$ is increased the ratio of electrostatic field energy to particle energy increases from 2×10^{-4} to 0.044. This is due to the grid aliasing of wavelengths which causes the spectral density to be larger at short wavelengths than in a real plasma [15]. As $\omega_{pe}\Delta t$ increases the electrostatic field energy decreases. For $\Delta x/\lambda_{De} = 20$ the electrostatic field energy decreases by a factor of 2500 as we go from minimum to maximum Δt. The reduction is due to the smoothing caused by simplified differencing which effectively reduces short wavelength fields by $1/(1 + (\omega_{pe}\Delta t)^2/2)$, and to the damping of high frequency oscillations caused by the implicit time advance.

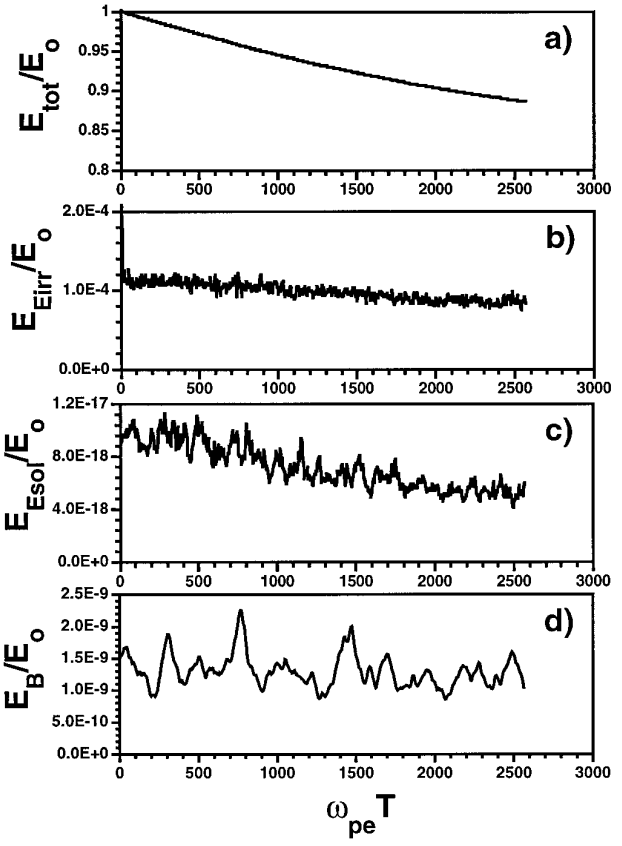

FIG. 3. Time histories of particle and field energies for a doubly periodic, uniform plasma DADIPIC simulation with $\Delta x/\lambda_{De} = 10.$ and $\omega_{pe}\Delta t = 5.$: (a) total system energy; (b) E_{irr} field energy; (c) E_{sol} field energy, and (d) B-field energy. All are normalized to the initial total system energy E_o. Notice the much smaller magnitude of the electromagnetic field energies compared to the electrostatic field energy.

As expected the energy in the electromagnetic fields is much smaller than the electrostatic field energy. Linear kinetic theory predicts the electromagnetic fluctuation field energy to be on the order of v^2/c^2 the electrostatic field energy [12]. For the DADIPIC plasma it is even less. For small Δt as we go from $\Delta x/\lambda_{De} = 0.2$ to 20, $E^2_{\text{sol}}/E^2_{\text{irr}} \sim 10^{-10}$ to 10^{-14}, and $B^2/E^2_{\text{irr}} \sim 10^{-5}$ to 10^{-8}. As the time step is increased E^2_{sol} does not decrease as fast as E^2_{irr}, and B^2 remains essentially constant. For large enough $\omega_{pe}\Delta t$ the B-field energy may even overtake the electrostatic field energy.

These simulations also provide a standard for algorithm timings. The code was run on the c machine (Cray 2) at the National Energy Research Supercomputer Center (NERSC). For the given simulation parameters a time step takes ~3.2 s. The portion of the time taken to complete

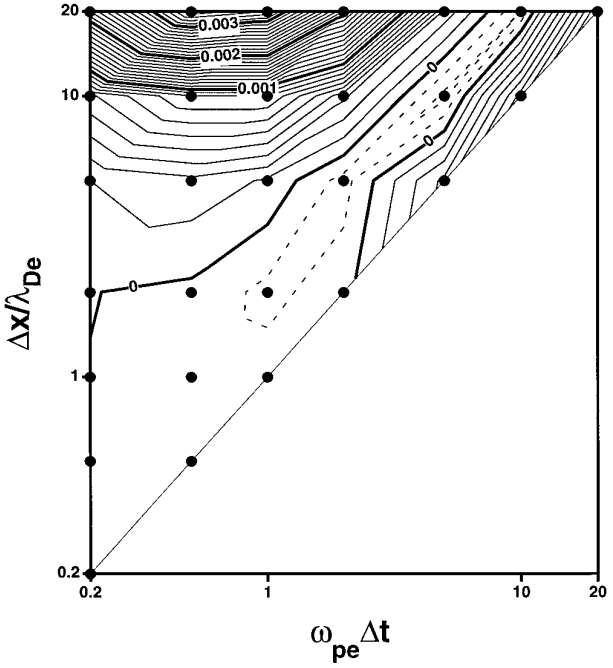

FIG. 4. Contour plot of $\Delta E/E_oN$ in $\Delta x/\lambda_{De}$ and $\omega_{pe}\Delta t$ space. The dots are the locations of the simulations run to generate the contours. The upper left hand region and the region near $v_{th}\Delta t/\Delta x = 1$ show heating. The region between with the dashed contours lines has cooling. Simulations were not run in the region where $v_{th}\Delta t/\Delta x > 1$.

the various components of a time step is 42% for particle operations, 25% for solution of the SDF equations, and 32% for solution of the implicit electrostatic field equation. Of course, these results serve as typical examples. For other simulations the time for particle operations should simply scale with the number of particles, but different boundary conditions and grid sizes effect the convergence of the DADI and biconjugate gradient routines. The solution of the fields may take a larger or smaller proportion of the run time as the simulation is changed.

These results can be used to compare DADIPIC to a fully electrodynamic, explicit PIC code. For an explicit code we can assume that solving for the fields would take negligible time. Because of the direct implicit particle advance, DADIPIC effectively has two particle pushes. So an explicit code would take half the time for particle operations. Thus we can expect that an explicit code would complete a time step five times faster than DADIPIC for a similar sized simulation. Of course, DADIPIC can run with much larger time steps and grid size than an explicit code. As a typical example consider a DADIPIC simulation with $\Delta x/\lambda_{De} = 30$ and $\omega_{pe}\Delta t = 10$. With an explicit code we would typically run with $\Delta x/\lambda_{De} = \omega_{pe}\Delta t = 0.2$. So DADIPIC would be able to run $(30/0.2) \times (30/0.2) \times (10/0.2)/5 = 225{,}000$ times faster for a 2D simulation with the same number of particles per cell as an explicit code. This neglects the huge expense in memory due to the factor of 22,500 more particles in the explicit simulation.

2. *Plot of the Numerical Change in Energy*

The contour plot of Fig. 4 shows the change in energy in the form $\Delta E/E_oN$, where ΔE is the change in the total energy over the simulation, E_o is the initial energy in fields and particles, and N is the number of time steps in the simulation. Table I has the results of the simulations which were interpolated to form the contour plot. The general trend is heating for large Δx due to the interpolation of the grid force [15] and cooling for large Δt due to the implicit electrostatic field solution. Simulations with and without the electromagnetic fields gave indistinguishable results for heating which is consistent with the relatively small magnitude of the electromagnetic fields. These results provide proof that the 2D Darwin, direct implicit combination does not lead to unexpected or unacceptable numerical heating or cooling. In fact, they are similar to Cohen *et al.* [16], where the 1D electrostatic direct implicit D_1 scheme was investigated. This is encouraging given that DADIPIC is a 2D electromagnetic scheme.

A difference between our results and theirs occurs in the region where $\Delta x/\lambda_{De} = \omega_{pe}\Delta t$. We believe the differ-

TABLE I

Change in Energy $\Delta E/E_oN$ in $\Delta x/\lambda_{De}$, $\omega_{pe}\Delta t$ Parameter Space

		$\omega_{pe}\Delta t$						
		0.2	0.5	1.0	2.0	5.0	10.0	20.0
$\frac{\Delta x}{\lambda_{De}}$	20.0	2.2e-3	3.5e-3	3.3e-3	2.1e-3	2.7e-4	−2.0e-4	1.0e-3
	10.0	4.8e-4	8.0e-4	8.0e-4	3.3e-4	−2.3e-4	6.5e-4	
	5.0	1.0e-4	1.7e-4	8.5e-5	−1.4e-4	3.3e-4		
	2.0	3.0e-6	−2.4e-5	−1.3e-4	−4.5e-5			
	1.0	−2.6e-6	−3.2e-5	−5.9e-5				
	0.5	−3.2e-6	−1.7e-5					
	0.2	−1.7e-6						

ences are the result of the type of simulations performed. Cohen *et al.* simulated periodic expanding plasma slabs and always observed cooling in the $\Delta x/\lambda_{De} = \omega_{pe}\Delta t$ region while in our uniform plasma simulations heating occurs in this region. The difference is in the initial state of the expanding slab with a step function in density. As shown in several sources [17] even for cases where the implicit solution eventually results in a net gain in total system energy, the behavior at early time is a decrease in total system energy. This is due to the effect of the implicit particle push on the spatially and temporally unresolved initial expansion of the slab. It the slab had been started with a slight slope to its sides the expansion would have been resolved and only the fluctuations in the densest part of the plasma would affect the change in total energy. The return of heating as $v_{th}\Delta t/\Delta x \simeq 1$ is due to the breakdown of the predictor–corrector solution for the electrostatic field. That solution depended on an expansion which is accurate only when particles move less than a cell in a time step.

As was stated in Section III our intent is only to quantify the impact of fluctuations assuming the other phenomena of interest are well resolved. With this qualification in mind, the contour plot can be used for any simulation by adjusting for the particle density, $n_p = 30{,}000\ \text{cm}^{-3}$, and plasma density, $n_o = 10^8\ \text{cm}^{-3}$, used here. The plot shows two contours where energy is conserved. Note the upper contour is a stable equilibrium. Plasmas with $\Delta x/\lambda_{De}$ below the contour will cool and move up to the contour. However, plasmas in the heating region to the right will continue to heat and reach the point where $v_{th}\Delta t/\Delta x > 1$. It is therefore advisable to run in the region, where $3v_{th}\Delta t/\Delta x \simeq 1$ in the densest part of the plasma. Parts of the plasma with lower densities will be at a point of smaller $\Delta x/\lambda_{De}$ and $\omega_{pe}\Delta t$ where energy is even better conserved.

Figure 5 has the final particle velocity distribution (dots) compared to the initial Maxwellian (dashed line) and a Maxwellian at the calculated temperature of the plasma at the end of the simulation (solid line) from several of the simulations used to generate the energy conservation contour plot. In all of these cases $\Delta x/\lambda_{De}$ is 10. The sequence of the plots is for increasing time step showing the effect of the first heating region (Fig. 5a), the energy conserving contour (Fig. 5b), the cooling region (Fig. 5c), and the second heating region (Fig. 5d). Figure 5e gives the distribution in the direction out of the simulation plane. Figure 5e provides computational evidence that there is no change in the distribution in the direction which has no $\mathbf{E}_{\text{irr}}$ indicating no other significant numerical heating or cooling mechanisms at work.

In the first heating region the particle distribution is mostly Maxwellian except at the largest velocities where the faster electrons appear somewhat cooled by the implicit particle advance. Along the energy conserving contour

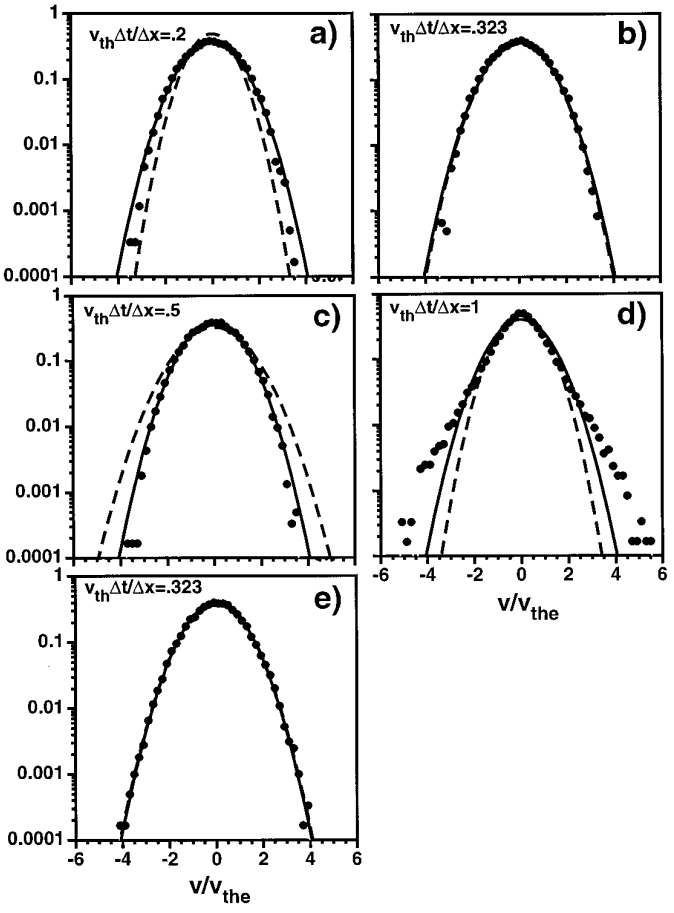

FIG. 5. Particle velocity distributions vs v/v_{th} resulting for different values of $\omega_{pe}\Delta t$: (a) in the first heating region, where $3v_{th}\Delta t/\Delta x \simeq 1$; (b) along the energy conserving contour, where $3v_{th}\Delta t/\Delta x \simeq 1$; (c) in the cooling region; (d) in the second heating region where $v_{th}\Delta t/\Delta x = 1$; and (e) in the direction out of the simulation plane.

the final distribution is not much different than the initial distribution. We have seen more pronounced changes for 1D simulations with a larger grid that were run for more time steps. A decrease in the tails and center of the distribution balanced by a bulging near the thermal velocity is observed. This indicates that faster particles are being cooled by the implicit advance while the slower particles are still heating due to the grid force. In the cooling region again the distribution remains essentially Maxwellian as the whole distribution cools due to the implicit particle advance. The only distribution which deviates substantially from a Maxwellian is that from the second heating region. Here the slower particles appear to remain near the initial distribution, but the faster particles heat dramatically. The heating appears to occur for those particles with speeds of v_{th} and above. In this region these are particles which are moving more than one cell in a time step. These results indicate that it is possible to use DADIPIC with large

TABLE II

Real, ω, and Imaginary, γ, Parts of the Frequency from the Darwin Dispersion Relation in a Constant B-Field

$\omega_{ce}\Delta t$	Analytic $\omega\Delta t$	PIC $\omega\Delta t$	Analytic $\gamma\Delta t$	PIC $\gamma\Delta t$
0.8	0.617	0.61	0.00244	0.0021
1.2	0.889	0.88	0.00965	0.0097
1.6	1.13	1.1	0.0227	0.021

temporal and spatial discretization while not causing large numerical affects to the particle velocity distribution. However, the constraint of a relationship between Δt and Δx must be met.

B. Uniform Plasma: Imposed Magnetic Field

As shown in Section III, the implementation of the Darwin method results in a scheme which is slightly unstable even at small Δt. In a previous paper [1] we investigated the ability of DADIPIC to reproduce linear electron cyclotron waves in magnetized plasma. We found that DADIPIC results agreed with analytic results for both the oscillation frequency and damping of these waves. In these simulations $\omega_{ce}\Delta t$ was kept at less than 0.4, and no adverse numerical instability effects were apparent. In addition, no problems with solution of the electrostatic field equation matrix were encountered on 32×32 grids. Here the effects of the numerical instability are quantified in simulations to gauge the applicability of the linear theory result of Section III for the actual code.

We ran a series of 1D periodic simulations with $\Delta x/\lambda_{De} = 10$ and $\omega_{pe}\Delta t = 3.1$, parameters which minimized numerical effects from the direct implicit scheme. The length of the simulations was 167 cm with 64 grid nodes. The plasma density of 1×10^8 cm^{-3} gave $ck_{\max}/\omega_{pe} = 2$, where $k_{\max}$ corresponds to the longest wavelength in the system. Larger wavenumbers are available, but as shown by Fig. 2 oscillations at such wavenumbers are less unstable. If the theoretical dispersion relation applies, only the longest wavelength in the system should grow noticeably. The simulations were run long enough to show a significant increase in the magnitude of the unstable mode (at least a factor of 20), the growth rate was calculated from an exponential curve fit to the B-field energy time history. The results are shown in Table II. The DADIPIC results agree with the linear theory to within a few percentages for both the oscillation frequency and growth of the instability indicating the reliability of the linear theory for predicting the effects of this instability. The dispersion relation can be used to set the time step with the goal of keeping the effect of the numerical instability small given the size of the system, the magnitude of the B-field, and the plasma frequency.

C. Large Density Gradients: Electron Beam Filamentation

Electron beam filamentation serves as the final doubly periodic test case for DADIPIC. In these tests density gradients, electrostatic fields, and electromagnetic fields are all significant. Consider a neutral plasma column aligned along the y axis with electrons flowing in the column. The electrons have two components uniformly distributed across the column, a dense target, T, flowing in the negative y direction and a faster beam, B, flowing in the positive y direction. This results in a Weibel-type electromagnetic instability in which the electron components breakup into filaments [18]. For the case where the total momentum in the system is zero and the electron components are at the same temperature the dispersion relation is [19]

$$(\omega^2 - k^2 v_{the}^2)(\omega^2 - \omega_{pe}^2 - c^2k^2) - k^2(\omega_{pT}^2 u_{oT}^2 + \omega_{pB}^2 u_{oB}^2) = 0. \tag{4.1}$$

A purely imaginary root to this equation, indicating growth of an instability, results when

$$\frac{kv_{th}}{\omega_{pe}} < \left[\sum_s \left(\frac{\omega_{ps}}{\omega_{pe}}\right)^2 \left(\frac{u_{os}^2}{c^2} - \frac{v_{th}^2}{c^2}\right)\right]^{1/2}. \tag{4.2}$$

So for any particular initial conditions the instability will only grow for certain wavelengths. As the transverse temperature increases, progressively longer wavelengths will become stable.

Two simulations were initialized to investigate this instability. The first was a uniform, doubly periodic plasma where the size of the simulation region sets the longest wavelength. This allows the electromagnetic instability to grow with minimal electrostatic effects. The second was a finite size column which could expand during the simulation. Here nonuniformity, electromagnetic, and electrostatic effects were significant at the same time. The parameters for these runs are 32×32 grid, $\omega_{pe}\Delta t = 10$, $\Delta x/\lambda_{De} = 48$, length of problem 395 cm, 30,000 particles of each species, ion density of 10^8 cm^{-3}, and 160 time steps. In these simulations the initial temperature was chosen to allow the heating due to the filamentation to increase λ_{De} and bring $\Delta x/\lambda_{De}$ to the energy conservation contour. The electron densities and velocities normalized to the ion density and the speed of light respectively are shown in Table III. Since the streaming velocities are in the y direction where there is no electrostatic field, the electrostatic two-stream instability will not occur. This significantly simplifies the interactions to be observed.

Figure 6 shows the B-field energy and particle energy for the uniform plasma and finite beam problems. The

TABLE III
Species Parameters for Filamentation Simulations

	Beam electrons	Target electrons	Ions
Density	1/11	10/11	1
v_{drift}/c	0.05	0.005	0
v_{th}/c	0.005	0.005	1.2×10^{-4}

beam energy ($KE_{\parallel}$) is converted into field energy and perpendicular thermal energy as the instability grows. Note that $KE_{\perp}$ does not grow as much in the finite beam case since not as large a v_{th} is required to move the stable point to k less than $k_{\min}$. The growth rate can be found quite easily from the slope of the initially linear increasing B-field energy on the log plots. The variation of linear theory grow rate with wavenumber is shown in Fig. 7. The horizontal lines in the figure are the results from simulation. The simulation results have been cut off at the maximum wavelengths attainable corresponding to the width of the simulation in the uniform plasma case and the width of the beam in the finite beam case. In both cases the size of Δx was set so that the shorter wavelengths available in the simulations would be stable. In the simulations the instability should grow at the largest rate within the band of available wavelengths. Considering the largest available linear theory growth rate, we see a variation of $\simeq$10% from the simulation results ($\gamma_{\text{PIC}} = 0.01\omega_{pe}$ vs $\gamma_{\text{theory}} = 0.0095\omega_{pe}$ for the finite beam case).

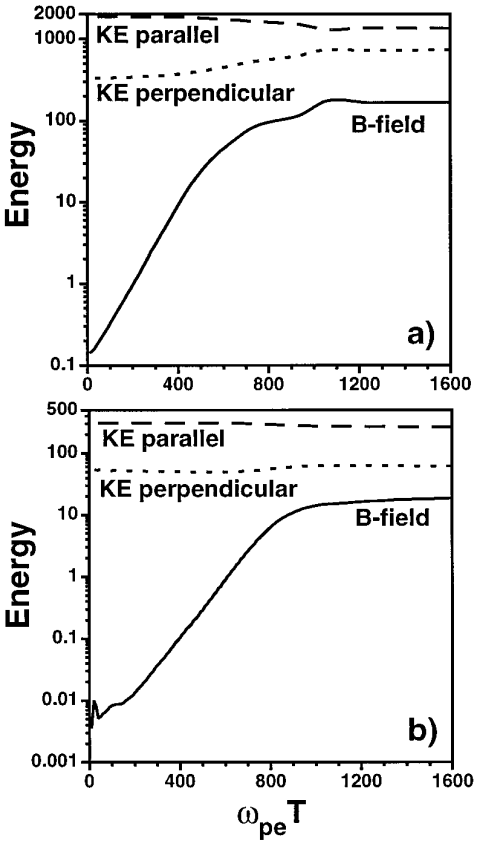

FIG. 6. Beam filamentation B-field and particle energies showing the exponential increase of the B-field during growth of the instability; (a) the uniform plasma and (b) the finite beam.

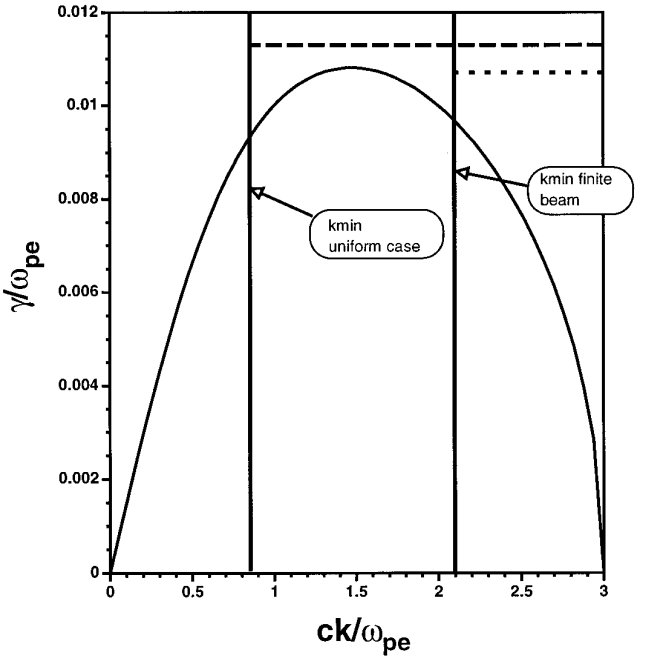

FIG. 7. Beam filamentation growth rates. The solid curve is the theoretical dispersion curve. The large dashed line (uniform plasma) and small dashed line (finite beam) show the grow rates observed in DADIPIC simulations. The lines extend to the minimum wavenumbers available in the simulations.

The fastest growing mode for the finite beam is also the longest wavelength which can fit within the beam width and the last mode to stabilize. The longest wavelength mode is thus the only mode to grow to perceptible size as shown in the particle plots of the beam and target electrons in Fig. 8, where the beam electrons have coalesced into a single filament. The uniform plasma, on the other hand, is wide enough to allow longer wavelength modes to continue to grow after the fastest mode has stabilized. This is evidenced by the second spurt of growth in the B-field energy. Figure 9 illustrates the change in mode with B-field plots at early and late time. At early time the fastest growing mode with $ck/\omega_{pe} = 1.5$ dominates while at late time the mode saturates at the longest wavelength available.

Finally, there is the question of whether any changes in energy due to numerical effects are important. Figure 10 has the time histories of the total energy for the two simula-

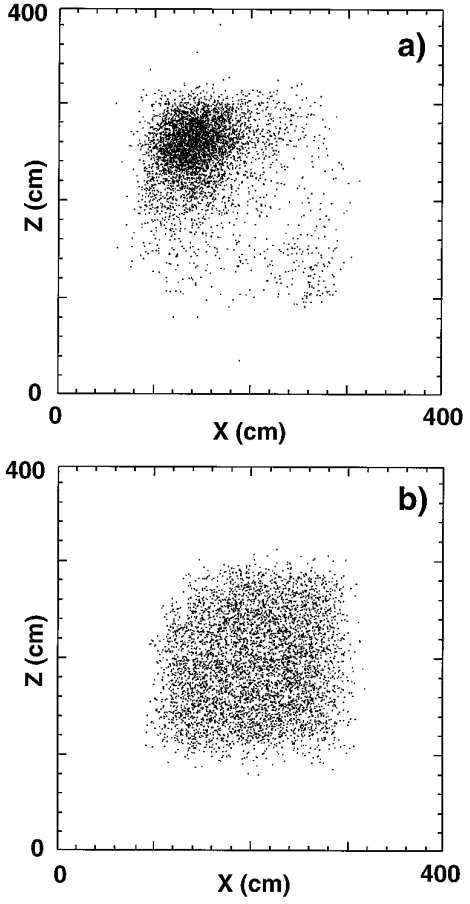

FIG. 8. Beam filamentation electron particle plots for the finite beam: (a) beam electrons and (b) target electrons. These are snaphots at $\omega_{pe}\Delta t = 1600$ after saturation of the instability, where the beam electrons have coalesced into one filament.

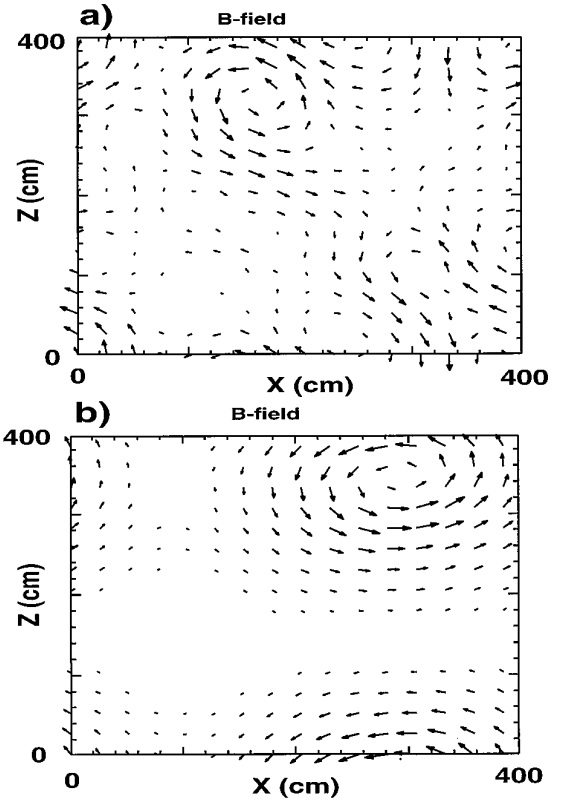

FIG. 9. Beam filamentation B-field plots for the uniform plasma showing a change in the unstable mode. (a) At early time, $\omega_{pe}\Delta t = 320$, a shorter wavelength has the fastest growth rate (longest vector = .0531 gauss). (b) At late time, $\omega_{pe}\Delta t = 1600$, the initial mode stabilizes and the slower growing longest wavelength mode dominates (longest vector = 0.356 gauss).

tions. In the uniform case the electrons are heated in the perpendicular direction by the instability. In the finite beam case the electrons are heated by the instability and cooled by the plasma column expansion. In both cases the change in temperature causes a change in $\Delta x/\lambda_{De}$ in the plnae of the electrostatic field. In addition to the heating effects, the B-fields have grown to significant size by the end of the simulations. We reach magnitudes where $\omega_{ce}\Delta t = 0.1$ and the off-diagonal terms in the implicit susceptibility tensor are 5% of the diagonal terms. However, in both cases the initial choice of $\Delta x/\lambda_{De}$ allowed the plasmas to remain near enough to the energy conservation contour to cause negligible change in the total energy (~2%) compared to the 60% change in the target electron thermal energy and 730% change in the beam electron thermal energy (uniform case). This results in $v_{th}\Delta t/\Delta x = 3.8$ and 1.8 at the end of the simulation for the target and beam electrons, respectively. Remember the energy conservation contour is approximately $v_{th}\Delta t/\Delta x = 3$. As shown by the excellent agreement with theory of the growth rates and mode wavelengths, any numerical effects did not adversely affect the final results.

These results may be compared to the fully electromagnetic, implicit code AVANTI which Hewett and Langdon [5] test with the same beam filamentation phenomena. For similar simulation particle numbers, grid sizes, and $v_{th}\Delta t/\Delta x$, DADIPIC appears to achieve better results. The change in energy for the AVANTI simulations was ~20%, a factor of 10 larger than the DADIPIC simulations. The growth rates, compared to analytic theory, were at best within a factor of two as opposed to the ~10% for DADIPIC. Results, such as these, along with the field solution and boundary condition concerns detailed in our previous paper [1], have convinced us to pursue DADIPIC for low frequency plasma simulation.

V. DADIPIC MODE OF OPERATION

The theory of Section III and its verification in Section IV lead u to some general guidelines to ensure stable and

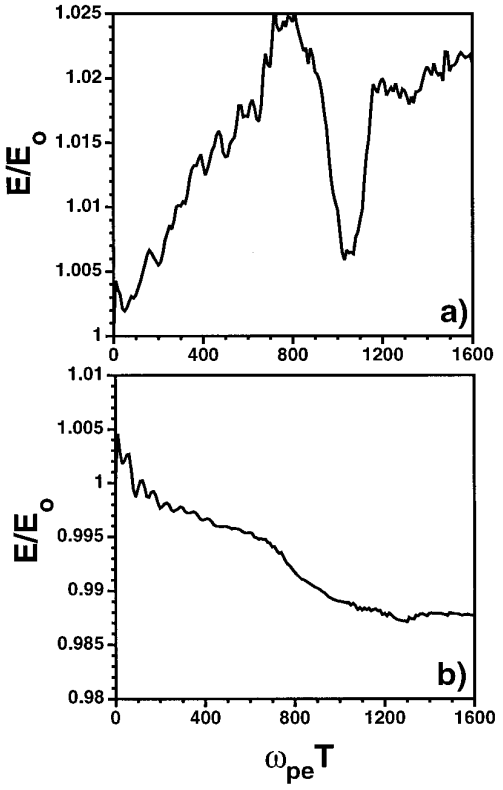

FIG. 10. Beam filamentation total system energy. Even with the large changes in T_e changes in the total system energy are 2% or less.

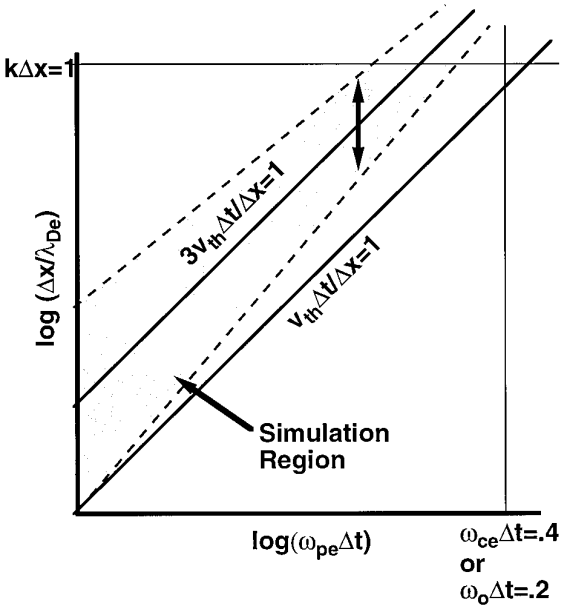

FIG. 11. Recommended operating region (shaded) for DADIPIC in the $\Delta x/\lambda_{De}$ versus $\omega_{pe}\Delta t$ plane. The width of the region depends on the tolerable numerical effect on electron kinetic energy. The region can extend to $\Delta x/\lambda_{De}$ and $\omega_{pe}\Delta t \gg 1$.

accurate DADIPIC simulation. These guidelines combine to give a region of operation in $\Delta x/\lambda_{De}$ versus $\omega_{pe}\Delta t$ space as shown in Fig. 11. In order to resolve the phenomenon of interest we are constrained by $k\Delta x < 1$ and $\omega_o\Delta t < 0.2$. The cyclotron instability requires $\omega_{ce}\Delta t < 0.4$ which may be more or less stringent a constraint than the requirement to resolve the low frequency phenomenon. We must stay near the line $3v_{th}\Delta x/\Delta t = 1$ to prevent numerical heating as well as ensure accuracy of the implicit field equation and particle accelerations. The width of the allowed region around the energy conserving contour depends on the amount of numerical heating which we can tolerate. Essentially we want to meet the condition

$$\Delta K\, E_{\text{numerical}}/\Delta K\, E_{\text{phenomena}} \ll 1. \tag{5.1}$$

In any particular simulation the change in the total kinetic energy due to the phenomena can be estimated. As the temperature of the plasma changes during a simulation the ratio $\Delta x/\lambda_{De}$ changes as represented by the vertical bar in Fig. 11. The numerical effect on the kinetic energy is given by

$$\Delta K\, E_{\text{numerical}} = \int \frac{\Delta E}{E_o N}\left(\frac{\Delta x}{\lambda_{De}}(t)\right) dt. \tag{5.2}$$

The bounding lines around the energy conserving contour are set by the condition of Eq. (5.1). The simulation is run where the bar for the change in $\Delta x/\lambda_{De}$ fits between the allowed limits due to numerical changes in energy.

With this method two different types of situations can be simulated. The first is equilibrium phenomena, where T_e remains basically unchanged (i.e., Section IV.A). Large, but nearly balanced, fluxes of energy into and out of the system are still possible. In this case the spatial and temporal discretization is set so the simulation resides on the energy conserving contour and the phenomenon of interest is resolved. Systems where the plasma temperature is changing can be handled by initializing the simulation so that the energy-conserving contour is crossed minimizing numerical heating/cooling effects (i.e., Section IV.C).

There are two schemes which may further minimize numerical heating/cooling and further increases the width of the simulation region. The time step could be varied dynamically during a simulation in order to stay near the energy conserving contour. An alternative is to implement a δf scheme [20] to minimize the electrostatic fluctuations which are the cause of the numerical change in kinetic energy.

VI. CONCLUSION

In this paper we have investigated the performance of the Darwin direct implicit particle-in-cell (DADIPIC)

method for the low frequency simulation of kinetic plasmas. In this investigation we have used linear theory and simulations to characterize the limits on spatial and temporal discretization for stable and accurate simulation. The algorithm, which we have implemented operates in agreement with linear theory in a 2D code. As intended DADIPIC eliminates the $c\Delta t/\Delta x < 1$ and $\omega_{pe}\Delta t < 2$ constraints of explicit, electrodynamic PIC. The cyclotron frequency must still be resolved, and the condition $3v_{th}\Delta t/\Delta x \sim 1$ must be met to minimize numerical heat/cooling. We developed relatively unrestrictive guidelines that allow the large space and time scale capabilities of DADIPIC to be applied successfully even in circumstances highly stressful to the algorithm (i.e., large density gradients, imposed magnetic fields, large electrostatic and electromagnetic fields).

ACKNOWLEDGMENTS

This work was performed under the auspices of the U.S. Department of Energy by the Lawrence Livermore National Laboratory under Contract W-7405-ENG-48.

REFERENCES

1. M. R. Gibbons and D. W. Hewett, *J. Comput. Phys.* **120,** 231 (1995).
2. A. B. Langdon and D. C. Barnes, *Multiple Time Scales,* Comput. Techniques Series (Academic Press, New York, 1985).
3. A. B. Langdon, B. I. Cohen, and A. Friedman, *J. Comput. Phys.* **51,** 107 (1983).
4. B. I. Cohen, A. B. Langdon, and A. Friedman, *J. Comput. Phys.* **56,** 51 (1984).
5. D. W. Hewett and A. B. Langdon, *J. Comput. Phys.* **72,** 121 (1987).
6. C. G. Darwin, *Phil Mag.* **39,** 537 (1920).
7. C. W. Nielson and H. R. Lewis, *Particle-Code Methods in the Nonradiative Limit,* Methods in Comput. Phys., Vol. 16 (Academic Press, New York, 1976).
8. D. W. Hewett and J. K. Boyd, *J. Comput. Phys.* **70,** 166 (1987).
9. P. J. Roache, *Computational Fluid Dynamics* (Hermosa, Albuquerque, NM, 1976), p. 42.
10. B. Noble and J. W. Daniel, *Applied Linear Algebra* (Prentice–Hall, Englewood Cliffs, NJ, 1977).
11. A. N. Kaufman and P. S. Rostler, *Phys. Fluids* **14,** 446 (1971).
12. N. A. Krall and A. W. Trivelpiece, *Principles of Plasma Physics* (San Francisco Press, San Francisco, CA, 1986).
13. R. W. Hockney, *J. Comput. Phys.* **8,** 19 (1971).
14. A. B. Langdon, *Phys. Fluids* **22**(1), 163 (1979).
15. C. K. Birdsall and A. B. Langdon, *Plasma Physics via Computer Simulation* (McGraw–Hill, New York, 1985).
16. B. I. Cohen, A. B. Langdon, D. W. Hewett, and R. J. Procassini, *J. Comput. Phys.* **81,** 151 (1989).
17. A. Friedman, *J. Comput. Phys.* **90,** 292 (1990).
18. E. S. Weibel, *Phys. Rev. Lett.* **2,** 83 (1959).
19. H. Momota, *Prog. Theor. Phys.* **35,** 380 (1966).
20. G. DiPeso, E. C. Morse, and R. W. Ziolkowski, *J. Comput. Phys.* **96,** 325 (1991).